Title

A Model-Based Approach for Determining Orientations of Biological Macromolecules Imaged by Cryoelectron Microscopy

Journal

Journal of Structural Biology, 116(1)

ISSN

1047-8477

Authors

Baker, Timothy S
Cheng, R Holland

Publication Date

1996

DOI

10.1006/jsbi.1996.0020

Peer reviewed

JOURNAL OF STRUCTURAL BIOLOGY **116,** 120–130 (1996)
ARTICLE NO. 0020

A Model-Based Approach for Determining Orientations of Biological Macromolecules Imaged by Cryoelectron Microscopy

TIMOTHY S. BAKER[1] AND R. HOLLAND CHENG

Department of Biological Sciences, Purdue University, West Lafayette, Indiana 47907-1392

Received May 18, 1995, and in revised form September 8, 1995

A polar Fourier transform (PFT) method is described that facilitates determination and refinement of orientations of individual biological macromolecules imaged with cryoelectron microscopy techniques. A three-dimensional density map serves as a high signal-to-noise model from which a PFT database of different views is generated and against which the PFTs of individual images are correlated. The PFT produces rotation-invariant data particularly well-suited for rapid and accurate determination of orientation parameters. The method relies on accurate knowledge of the center of symmetry and radial scale of both model and image data but is insensitive to the relative contrast and background values of these data. Density maps may be derived from a variety of sources such as computer-generated models, X-ray crystallographic structures, and three-dimensional reconstructions computed from images. The PFT technique has been particularly useful for the analysis of particles with icosahedral symmetry and could be adapted for the analysis of single particles of any symmetry for which a crude model exists or can be produced.

INTRODUCTION

A critical step in determining reliable three-dimensional (3D)[2] structures of biological macromolecules from transmission electron micrographs involves identifying particle orientations so particle images can be properly combined and averaged (e.g., Lake, 1972; Misell, 1978; Moody, 1990). This task is generally straightforward for highly crystalline specimens whose translational symmetry makes it relatively easy (in Fourier transforms of images) to define the crystal symmetry elements and their orientations relative to the view direction. For noncrystalline specimens (particles) with either no internal symmetry such as the ribosome or with high internal symmetry such as the icosahedral viruses, the determination of the view orientations for individual, unstained particles from a noisy, low-dose electron micrograph is often problematic. The method of "Common Lines" (Crowther, 1971), in principle, may be used to determine the view orientations of specimens of *any* symmetry, but, in practice, the method has been most effective in the analysis of specimens with high internal symmetry such as the icosahedral viruses with their 60-fold redundancy (e.g., Crowther *et al.*, 1970; Crowther and Amos, 1972; Baker, 1992). The original Common Lines method works well with high-contrast images from nega-

[1] To whom correspondence should be addressed. Fax: (317)496-1189; Internet: tsb@bragg.bio.purdue.edu.

[2] Abbreviations used: B19, human parvovirus serotype 19; CaMV, cauliflower mosaic virus; CCMV, cowpea chlorotic mottle virus; $CCMV_E$, reassembled expressed CCMV capsid protein; $CCMV_{RNA1}$, CCMV reassembled with RNA1; $CCMV_S$, swollen CCMV; CMV, cucumber mosaic virus; CPMV, cowpea mosaic virus; CPSMV, cowpea severe mosaic virus; CPV, canine parvovirus; CRPV, cottontail rabbit papilloma virus; cryoEM, cryoelectron microscopy; dsDNA, double-stranded DNA; FHV, Flockhouse virus; FHV_{C74}, FHV N363T mutant; HPV-1, human papilloma virus, serotype 1; HPV_{L1}, HPV-1 assembled capsids of expressed L1 protein; HPV_{L1L2}, HPV-1 assembled capsids of expressed L1 and L2 proteins; HRV, human rhinovirus; HRV16-$ICAM_2$, HRV16 complexed with 2-domain ICAM; HRV16-$ICAM_5$, HRV16 complexed with 5-domain ICAM; ICAM, Intercellular adhesion molecule 1; ISVP, Intermediate subviral particle; L-A, L-A virus of *Saccharomyces cerevisiae;* NβV, *Nudaurelia capensis* virus; NOV, nodamura virus; PBCV, *Paramecium bursaria* chlorella virus; PFT, polar Fourier transform; Polyoma T = 1, reassembled polyoma VP1, T = 1 particle; $Reovirus_L$, Reovirus (T1 Lang serotype); $Reovirus_DV_E$, Reovirus (T3 Dearing serotype) virion (empty); $Reovirus_DISVP_E$, Reovirus (T3 Dearing serotype) ISVP (empty); $Reovirus_DC$, Reovirus (T3 Dearing serotype) core; $Reovirus_DC_E$, Reovirus (T3 Dearing serotype) core (empty); $Reovirus_LV_{CR}$, Reovirus (T1 Lang serotype) virion (center removed); $Reovirus_L$-$ISVP_{CR}$, Reovirus (T1 Lang serotype) ISVP (center removed); $Reovirus_LC$, Reovirus (T1 Lang serotype) core; $Reovirus_LC_{CR}$, Reovirus (T1 Lang serotype) core (center removed); RRV, Ross river virus; ssDNA, single-stranded DNA; ssRNA, single-stranded RNA; SV40, simian virus 40; UmV, P4 virus of *Ustilago maydis;* X-ray, X-ray crystallographic 3D model; ϕX174, bacteriophage ϕX174; $\phi X174_{PV}$, bacteriophage ϕX174 provirion; $\phi X174_{PC}$, bacteriophage ϕX174 procapsid; 1D, one-dimensional; 3D, three-dimensional.

1047-8477/96 $18.00

tively stained specimens, but can lead to inconsistent results when applied to low-contrast, noisy images of unstained, vitrified specimens (e.g., Fuller *et al.*, 1995). A statistical method that helps overcome some limitations of this method was developed by Fuller (1987), whose "Modified Common Lines" method is described elsewhere in this issue (Fuller *et al.*, 1996).

Here we describe a Polar Fourier Transform (PFT) method that was developed for use either in conjunction with Modified Common Lines or for *de novo* determination of particle orientations. The PFT method has been used by us as well as others to determine the structures of several icosahedral viruses (e.g., Dokland and Murialdo, 1993; Cheng *et al.*, 1994a,b, 1995; Hagensee *et al.*, 1994; Kenney *et al.*, 1994; Venién-Bryan and Fuller, 1994; Wikoff *et al.*, 1994; Fuller *et al.*, 1995; Ilag *et al.*, 1995; Zhao *et al.*, 1995). The method could also be adapted for the analysis of asymmetric macromolecules or those with lower symmetry than an icosahedron. A number of other alignment methods that use reference data in analogous ways to the PFT method have been independently developed (e.g., Harauz and van Heel, 1986; Crowther *et al.*, 1994; Penczek *et al.*, 1994; Radermacher, 1994). A detailed comparison of these and the PFT methods is beyond the scope of this article.

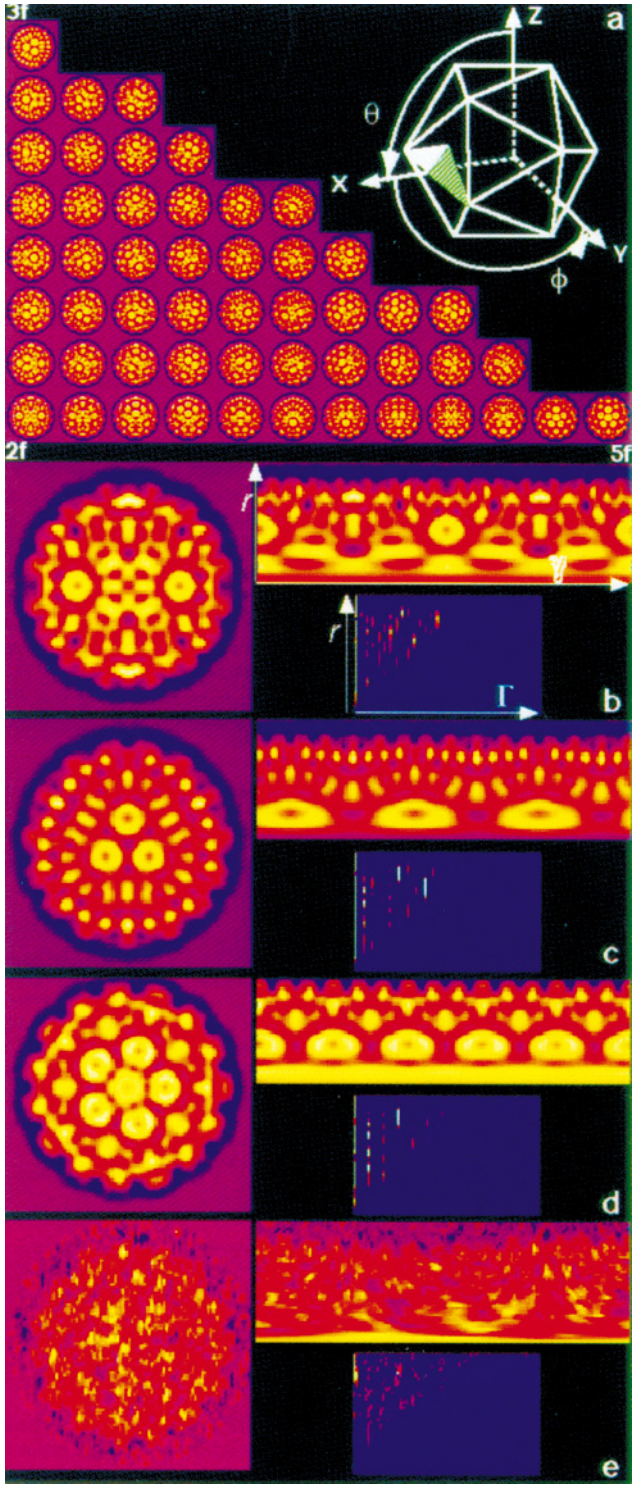

FIG. 1. Schematic representation of generation of PFT data for model (a–d) and raw image (e) data. (a) Fifty-two views of an SV40 3D reconstruction (Baker *et al.*, 1988, 1989), obtained by back-projecting the density map in 3° angular increments for orientations covering one-half of the icosahedral asymmetric unit: three-fold view at top left, two-fold at bottom left, and five-fold at bottom right (shaded, half-triangle in inset). Note that 382 views would be obtained if the model was viewed at finer angular intervals (~1°) as is normally done in the initial stage of a PFT refinement. Inset shows the standard convention (Klug and Finch, 1968) in which the icosahedron is aligned with three of its two-fold axes coincident with an *x,y,z* Cartesian coordinate system. Three angles define the orientation of the view direction: θ (rotation in the *xz* plane, positive from *z* toward *x*), ϕ (rotation in the *xy* plane, positive from *x* towards *y*), and ω (not depicted, defines the rotation of the object about the θ,ϕ view direction). (b) (Left) Two-fold view (θ,ϕ,ω = 90°,0°,0°) of SV40 model; (top right) the same view of SV40 but resampled onto a polar grid (radius, *r*, increases from bottom to top and azimuthal angle, γ, increases from left to right); (lower right) representation of PFT amplitude distribution (*r* increases from bottom to top and angular frequency, Δ, increases from left to right). Each row of the PFT is a 1D Fourier transform of the density distribution within the corresponding row (*r*) of the polar data. (c and d) The same as (b) for three-fold (θ,ϕ,ω = 69.1°,0°,−90°) and five-fold (θ,ϕ,ω = 90°,31.8°,−90°) views of the SV40 model, respectively. (e) The same as (b–d) for a raw image of an SV40 particle viewed close to a five-fold axis (θ,ϕ,ω = 89.9°,−31.4°,20.8°). All panels employ the same color table with brightest colors used to represent highest projected density (images, projections, and polar images and projections) or amplitude (PFT data).

METHODS

Projection and Polar Projection Reference Databases

Analysis of icosahedral particles with the PFT method begins with a 3D model from which m different projected views are generated to produce a reference database (Fig. 1a). For icosahedra, these views cover one-half of the asymmetric unit of the structure (e.g., 1/120th of an icosahedron from $\theta = 69$ to 90° and $\phi = 0$ to 32°). Each Cartesian view (x,y) is interpolated onto a polar grid (r,γ), which subdivides the data onto a series of equal-spaced annuli, from $r = 0$ to a radius just outside the particle edge (Figs. 1b–1e). The width of each annulus is equal to the sampling interval (pixel size) in the Cartesian data and all annuli are sampled the same number of times (γ direction) at a spacing fine enough to ensure that no loss of information occurs at high radii (i.e., sampling at least as fine as in the Cartesian image). The resultant polar data consist of the annuli organized in rows (r direction), all sampled the same number of times (γ direction). Hence, the polar data are oversampled at small r.

Computation of PFT Database and Initial Origin Determination for Particle Images

Each of the polar projections and images is Fourier transformed along the azimuthal (γ) direction to produce a database of PFTs (Figs. 1b–1d) against which the PFT of each "raw" image (Fig. 1.e) is correlated according to the scheme depicted in Fig. 2. Thus, the PFT representation is simply a series of one-dimensional (ID) Fourier transforms or rotational power spectra (Crowther and Amos, 1971), one for each annulus of data. This type of representation has the advantage of being rotation invariant (Schatz and van Heel, 1990) which greatly reduces the subsequent number of computations required to identify orientation parameters. Such data reduction leads to successful implementation of the PFT procedure only if an accurate starting estimate of the position of each particle origin known. This origin, where the icosahedral 2-, 3-, and 5-fold symmetry axes meet, is precisely defined for model data, but must be determined for each raw image.

An initial origin estimate $(x_o,y_o)_j$ for each virus image is obtained by first summing all projected views to produce an averaged projection, then circularly symmetrizing this average about its known center to produce a reference, and finally cross-correlating this reference against each of the n images (Fig. 2, dashed arrows). Experience shows that this procedure is quite reliable with spherical objects, probably because the projected image of a sphere (a circular disk) is centrosymmetric and thus has a well-defined center.

Scaling

The model and image data must be within a few percent of the same magnification for the PFT method to succeed. One way to check the relative scales of the data is to compare ID radial density plots (e.g., Olson and Baker, 1989; Belnap *et al.*, 1993) of the circularly symmetrized reference projection (Fig. 2) and a circularly symmetrized, global average of the images. If necessary, the magnification of the 3D model is adjusted accordingly and the particle image origins are redetermined (Fig. 2, dashed arrows). The absolute contrast and average density of the model and image data need not be carefully scaled because the correlation procedures are insensitive to differences in these characteristics except that the relative contrast of the model and image data must be of the same sign.

Determination of Orientation (θ,ϕ,ω) and Origin (x,y) Values

Each of the image PFTs is correlated in turn with all model PFTs to identify which model PFT best matches each image PFT (Fig. 2). This process provides an initial estimate of the values of θ and $|\phi|$ for each image. The rotation angle, ω, and the sign of

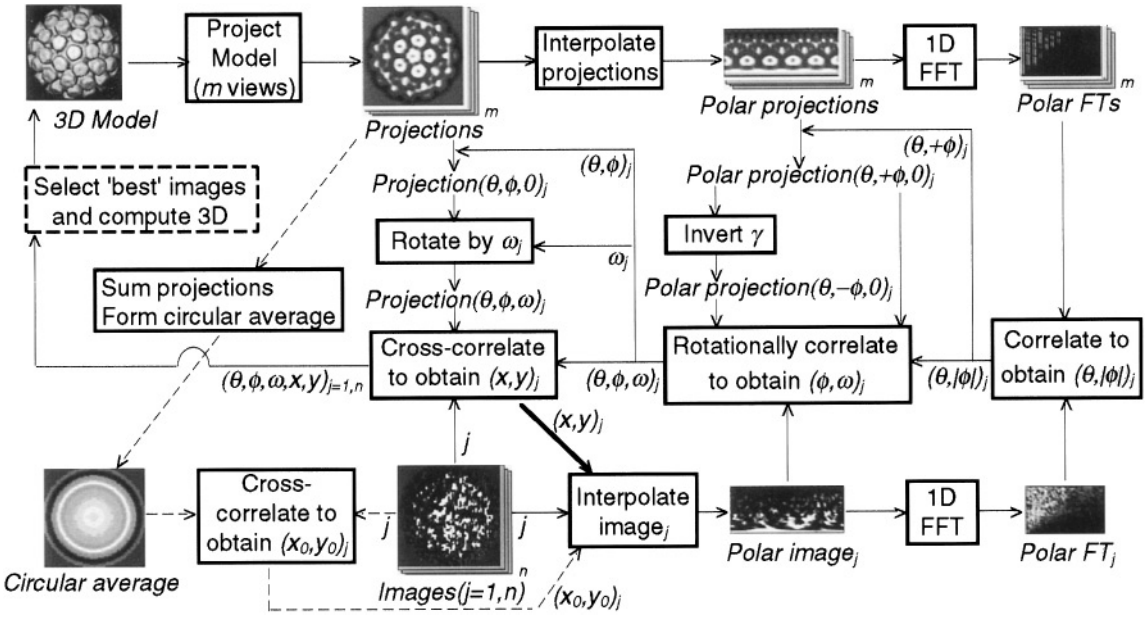

FIG. 2. Schematic diagram of EMPFT procedure. The process typically begins by computing a series of m projections from the 3D model (top row) at 1° angular intervals followed by determination of initial origins of the particle images (dashed arrows). Then, the polar coordinate interpolations, Fourier transformations, and various correlations of the data are performed as indicated (solid arrows), leading to values of θ,ϕ,ω,x,y for each of the n images. A "best" subset of these images is used to compute a 3D reconstruction (dashed box) and the entire process may be repeated with this new model. Either new particle origins may be determined (dashed arrows) or the newly acquired origin coordinates may be used (thick arrow). Continued cycles of refinement may include the use of 3D models computed from different subsets of images, computation of projections at finer angular increments, and addition of higher resolution data. See text for detailed description of the steps.

ϕ, which are consistent with the hand of the 3D model, are derived from the rotational correlations (γ direction) computed between polar image$_j$ and polar projection$(\theta,+\phi,0)_j$ and polar projection$(\theta,-\phi,0)_j$ (Fig. 2). Knowledge of $(\theta,\phi,\omega)_j$ allows more accurate refinement of the particle origin via translational cross-correlation between image$_j$ and model projection$(\theta,\phi,0)_j$ after it is rotated by ω_j to give projection $(\theta,\phi,\omega)_j$ (Fig. 2).

New Model and Subsequent Refinement

With view directions and origins known for all n images, a 3D reconstruction can be computed by means of Fourier-Bessel procedures (Fuller *et al.*, 1996) (Fig. 2). Normally, only those images that correlate best with the model data (usually $<<n/2$) are used. This reconstruction serves as a new 3D model for an additional cycle of refinement of the θ,ϕ,ω,x,y parameters as already described (Fig. 2; all steps except thick arrow). Alternatively, one can use the (x,y) origins determined in the previous cycle to compute each new polar image (Fig. 2; thick arrow) rather than recomputing a new set of origin estimates (x_o,y_o) (Fig. 2; dashed arrows). Refinement can proceed by calculating a new set of model projections on a finer grid of θ and ϕ values, and these are typically computed within a 7 by 7 grid with $\Delta\theta$ and $\Delta\phi = 0.5°$ and centered about the θ and ϕ values determined in the last cycle.

Enhanced Refinement with Filtered Data

Refinement is repeated until no further increases in the correlation coefficients can be obtained between image$_j$ and model projection$(\theta,\phi,\omega)_j$, between PFTj and projection PFT$(\theta,|\phi|)_j$, or between polar image$_j$ and polar projection$(\theta,|\phi|,0)_j$ (Fig. 2). These tests are sensitized by screening out selected data from the comparisons. For example, the outermost radii of the projected images of most spherical viruses contain the maximum "icosahedral signal," whereas lower radii contain less "signal" because the center of the projection images includes large contributions from the projected density of the virus cores, which typically consist of disordered genomic material. The influence of the non icosahedrally ordered density is minimized by correlating only the high radii features which mainly correspond to the icosahedrally ordered protein capsids. Likewise, the lower radii density in the 3D reconstructions used as model data are usually zeroed as a means to further enhance the success of the PFT procedure. This is especially useful when either single-particle or extreme defocus reconstruction models are used (S. Fuller, personal communication).

Azimuthal frequencies can be filtered out of the PFTs to enhance the correlation analysis between the model and image PFTs (Fig. 2). For example, the circularly symmetric, zero-order, and other low-order components, which dominate the PFT data (Figs. 1b–1e; leftmost columns in each PFT representation) yet do nothing or very little to specify orientation, are usually ignored during computation of the correlation coefficients. Also, some of the highest-order components, which are dominated by high-frequency noise, are filtered out.

EMPFT Program

The VAX/VMS FORTRAN program, EMPFT, performs all the operations illustrated in Fig. 2 except for the selection of "best" images and computation a new 3D model (dashed box). EMPFT has been implemented at Purdue on Digital VAX and AXP platforms and the FORTRAN code is freely distributed by contacting either author (tsb@bragg.bio.purdue.edu; rhc@bragg.bio.purdue.edu). Others have ported this code to UNIX platforms (e.g., Fuller *et al.*, 1996). Program input consists of a 3D density map in Purdue INTEGER*2 or REAL*4 MAP format and the entire set of raw images are packed in a single file in Purdue BYTE IMG format. 3D icosahedral reconstructions were produced with the package of programs described by Fuller *et al.* (1996). Computer-generated models were produced with programs similar to those described by Rayment *et al.* (1983). Low-resolution X-ray models were generated from atomic coordinate data as described by Cheng *et al.* (1994b). Output consists of a number of ASCII format data files that list several different correlation coefficients between model and raw data and an ASCII format file that contains the list of θ,ϕ,ω,x,y, and other parameters that serve as a standard input file for many of the icosahedral reconstruction programs (Fuller *et al.*, 1996).

RESULTS AND DISCUSSION

PFT Method

The PFT method relies on the use of a 3D model to screen noisy images of individual particles and refine a set of θ,ϕ,ω,x,y parameters to enable a 3D reconstruction to be computed from the set of images. A major advantage of the PFT method, like that of other model-based methods (e.g., Crowther *et al.*, 1994; Penczek *et al.*, 1994; Radermacher, 1994), is that the raw image data are compared to relatively noise-free, 3D model data rather than other noisy data as is done in the Common Lines (Crowther, 1971) and the Modified Common Lines (Fuller, 1987) techniques. Additionally, the PFT method makes use of *all* of the available data if so desired, whereas the Common Lines only sample a fraction of Fourier data and this fraction progressively decreases at high resolution (Fig. 3; see also Fuller *et al.*, 1996).

These advantages of the PFT method have led to more consistent results in our analyses of virus images when compared to our use of Common Lines methods. Common Lines often fails or leads to inconsistent results with cryoEM images recorded close to focus (<1.5 μm) or with viruses that do not have coarse morphological features (see Example 4, below). Our Common Lines analysis of CaMV only succeeded after we recorded focal pairs of vitrified specimens and used a 2.4-μm underfocus micrograph to determine initial orientations of the particles and applied these values to the same particles in the closer-to-focus (1.2-μm), lower-dose image (Cheng *et al.*, 1992). As a test, we reexamined the same 1.2-μm image with Common Lines and were only able to identify the correct orientation view for 1 of the 21 CaMV particle images that went into the original 3D reconstruction. Similarly, the success rate of Common Lines in finding orientations of low pH-treated Semliki Forest viruses was less than 10% (Fuller *et al.*, 1995). We have now used the PFT method to successfully examine a large number of viruses from micrographs recorded at $\leqslant$1.5 μm defocus (Cheng *et al.*, 1994a,b, 1995; Hagensee *et al.*, 1994; Wikoff *et al.*, 1994; Ilag *et al.*, 1995; Zhao *et al.*, 1995).

The degeneracy of the common lines for particles oriented near one of the icosahedral symmetry axes often makes it very difficult to correctly identify such particles with confidence (Fuller, 1987). Hence,

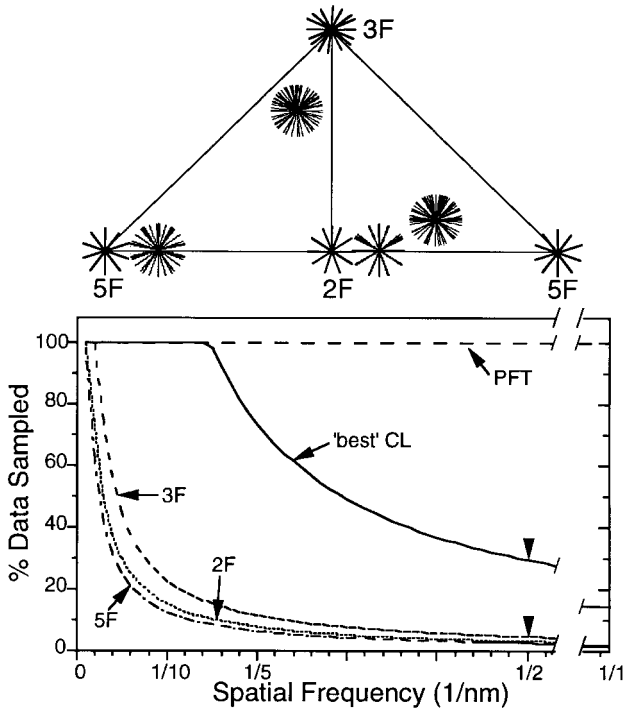

FIG. 3. Fourier sampling in PFT and Common Lines methods. (Top) Distribution of the 37 pairs of common lines in Fourier space for several different orientations of an icosahedral particle are depicted within the triangular icosahedral asymmetric unit. The spread of common lines is quite limited for the 2-, 3-, and 5-fold orientations and for an orientation close to the 2-fold (at θ,ϕ,ω = 90°,2°,0°). Orientations further from the symmetry axes (θ,ϕ,ω = 75°, −5°,0; 88°,15°,0°; and 90°,−27°,0°) have more uniformly spread common lines which provide more complete sampling of Fourier space, especially at low resolution. (Bottom) Plots comparing the fractions of Fourier data sampled with the PFT and Common Lines methods. The amount of Fourier data sampled by the common lines for the three different axial orientations rapidly drops as a function of spatial frequency such that only 3–4% of the data are sampled at 20 Å (arrowhead) and less than 2% are sampled at 10 Å resolution. In a hypothetical, "ideal" situation, where the common lines are uniformly spread, all of the Fourier data are obtained out to ~60 Å but only ~30% (arrowhead) and ~15% of the data are sampled at 20 and 10 Å, respectively. In contrast, 100% of the Fourier data is accessible to the PFT procedure.

even though the quality of the images of such particles may be quite good, these data are usually omitted from the computation of the 3D reconstructions. The PFT method appears to have no orientation bias and we have repeatedly found that this method correctly identifies a high percentage of particles that would have been rejected in a Common Lines analysis (data not shown). In addition, the Modified Common Lines and PFT methods are better able than Common Lines to discriminate between the relative handedness of the projection images obtained from different particles (e.g., Conway *et al.*, 1995).

A significant advantage of the PFT method is the relative speed with which the orientations and origins of a large number of particle images can be determined. This efficiency is partly a consequence of greatly reduced computations needed for the PFT method compared to the Common Lines methods (Crowther, 1971; Fuller, 1987), especially when larger size data sets (>50–100 particle images) are analyzed. For PFT, the computations increase linearly with the number of particle images. Common lines and cross-common lines algorithms (Crowther, 1971; Fuller, 1987) on the other hand, require computations that increase in number at a faster rate than the number of images and hence, even the use of massively parallel computers (Martino *et al.*, 1994) may not provide a practical solution to the analysis of very large data sets (>1000 images). A more significant, though less easily quantified, advantage of the PFT method is that it requires much less user intervention compared to the Common Lines methods. The poor success rate in determining good initial estimates of particle orientations with Common Lines necessitates an often tedious process of examining the data for each particle individually and using various criteria to select the most promising particle images for cross-common lines analysis (Fuller, 1987; Fuller *et al.*, 1996).

The Model

The main restriction of the PFT method is the requirement for a "good" starting 3D model. However, the generation of a suitable model is often not a major obstacle in practice.

Initial model data can be generated in a variety of ways. The method chosen usually depends on the particular nature of the specimen being examined. We have used density maps from (1) simple, computer-generated, icosahedral models; (2) 3D reconstructions of structures expected to closely resemble the virus under investigation; (3) 3D reconstruction of the virus computed from a *single* particle image; and (4) an atomic model of the same or similar virus. Thus, the PFT method is analogous in principle to the molecular replacement method (Rossmann, 1972), which is extensively used to aid the phasing of X-ray crystallographic data of viruses and other macromolecules. Several illustrative examples of the use of the PFT method are presented below.

Example 1: Computer-Generated T = 7 Model—Analysis of CaMV

For some viruses like the dsDNA animal papovaviruses and the dsDNA plant caulimoviruses, a very simple computer model serves as a useful starting point for the PFT analysis (Figs. 4a–4c) because these viruses have capsids composed of large morphological units (capsomers) arranged on an enantiomorphic, T = 7 icosahedral lattice (Caspar and

Klug, 1962). A model with 72 spheres arranged on a T = 7*l* (left-handed) lattice (Fig. 4a1) and with overall dimensions adjusted to give an effective diameter of ~52 nm was used to initiate refinement of a set of 20 cryoEM images of CaMV. The subsequent models obtained during seven cycles of PFT refinement (Figs. 4a2–4a8) show how they converge to a final and correct solution. The starting model contains only very-low-resolution information (spheres) yet the final reconstruction shows 12 capsomers with pentameric substructure and 60 capsomers with hexameric substructure as was discovered in the original analysis of this structure (Cheng *et al.*, 1992). Correlation coefficients computed in reciprocal (Fig. 4b and in real (Fig. 4c) space demonstrate that the agreement between the raw and model data improves during refinement.

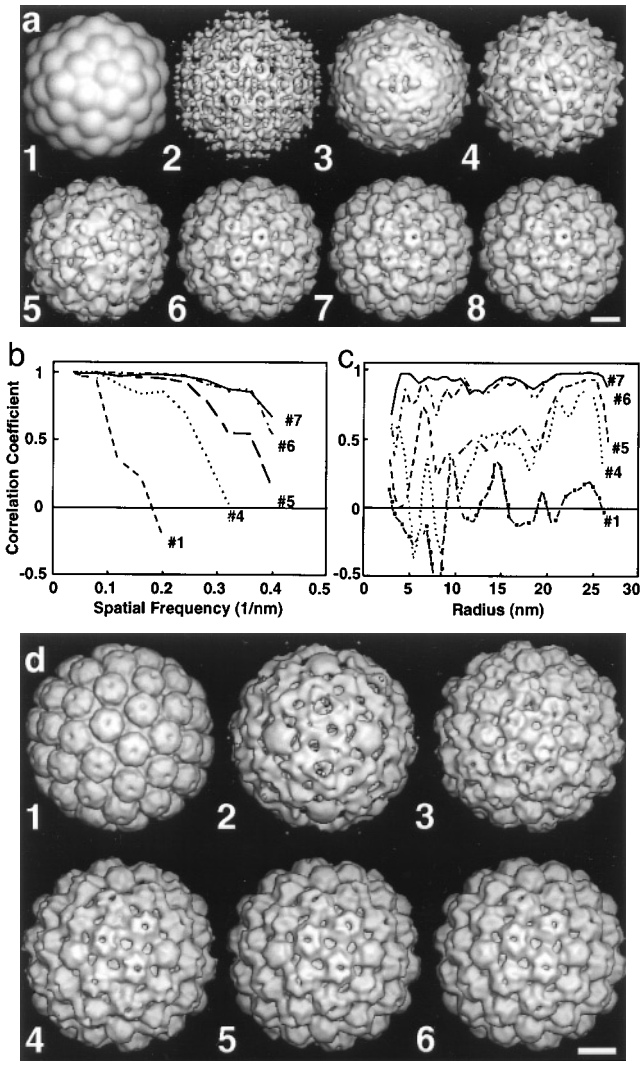

FIG. 4. (a) Refinement of CaMV with computer-generated, T = 7*l* model. (a1) 72-sphere, T = 7*l* computer model used for initiation of PFT refinement of CaMV images. (a2–a8) CaMV reconstructions obtained during seven cycles of refinement. (a8) Final CaMV reconstruction at 2.5 nm resolution computed from 20 images. (b–c) correlation coefficient plots computed after cycles 1, 4, 5, 6, and 7 of the refinement: the refined models and the original, 21-particle reconstruction of CaMV obtained by Common Lines (Cheng *et al.*, 1992) are compared in reciprocal space (b) and real space (c). In figures 4–10, shaded-surface representations of models and reconstructions are all viewed along an icosahedral 2-fold axis of symmetry. (d) Refinement of CaMV with polyoma starting model. (d1) 2.2-nm resolution X-ray model (Griffith *et al.*, 1992). (d2–d6) CaMV reconstructions obtained during five cycles of refinement. (d6) Final CaMV reconstruction computed from 20 images. Bars, 10 nm.

Example 2: Polyoma Model—Analysis of CaMV

Polyoma virus (~50 nm diameter) has 72 *pentameric* capsomers arranged on a T = 7*d* lattice (Rayment *et al.*, 1982). Given the close similarities in size and gross morphology of polyoma and CaMV, we used the 2.2-nm resolution X-ray structure of polyoma (Griffith *et al.*, 1992) as a model (Fig. 4d1) to refine the CaMV data set used in Example 1 above. The CaMV pentamer–hexamer structure again emerges despite the potential incorrect bias of the *all pentamer* polyoma model (Fig. 4d). This result is analogous to experiments in which various incorrect models were used to phase polyoma X-ray data and these all led to the same, correct solution (Rayment *et al.*, 1983). Note that the CaMV reconstruction ends up right-handed (T = 7*d:* Fig. 4d6) like the polyoma model (Fig. 4d1). In Example 1, the CaMV ended up left-handed (T = 7*l*: Fig. 4a8) like the computer model (Fig. 4a1). Thus, the starting model dictates the handedness of the final reconstruction because there is no *a priori* knowledge of handedness in the projected images themselves. A correct determination of the absolute hand of the reconstruction must be derived from other sources of information such as might be obtained by tilting experiments in the microscope (e.g., Klug and Finch, 1968; Finch, 1972; Cheng *et al.*, 1995) or by comparison with atomic resolution data (e.g., McKenna *et al.*, 1992; Olson *et al.*, 1993; Smith *et al.*, 1993a,b; Cheng *et al.*, 1994b; Porta *et al.*, 1994; Wikoff *et al.*, 1994; Ilag *et al.*, 1995). Nonetheless, despite the handedness ambiguity, the fine details of the structure emerge from the data and not from the model.

Example 3: CPMV Model—Analysis of ϕX174 and Vice Versa

A third test of the PFT routines involved the use of 3D reconstruction data for a virus different from the one being examined (Figs. 5a and 5b). CPMV is a ssRNA plant virus with an outer capsid that ranges in diameter from 25.4 to 30.8 nm (Stauffacher *et al.*, 1987) and ϕX174 is a ssDNA bacteriophage with an outer capsid that ranges in diameter from 24.7 to 33.0 nm (McKenna *et al.*, 1992; Olson *et al.*, 1992; Ilag *et al.*, 1995). At first glance these two viruses appear quite similar with prominent "caps" of density at the 12 icosahedral vertices. Closer inspection reveals many striking differences in the capsid sub-

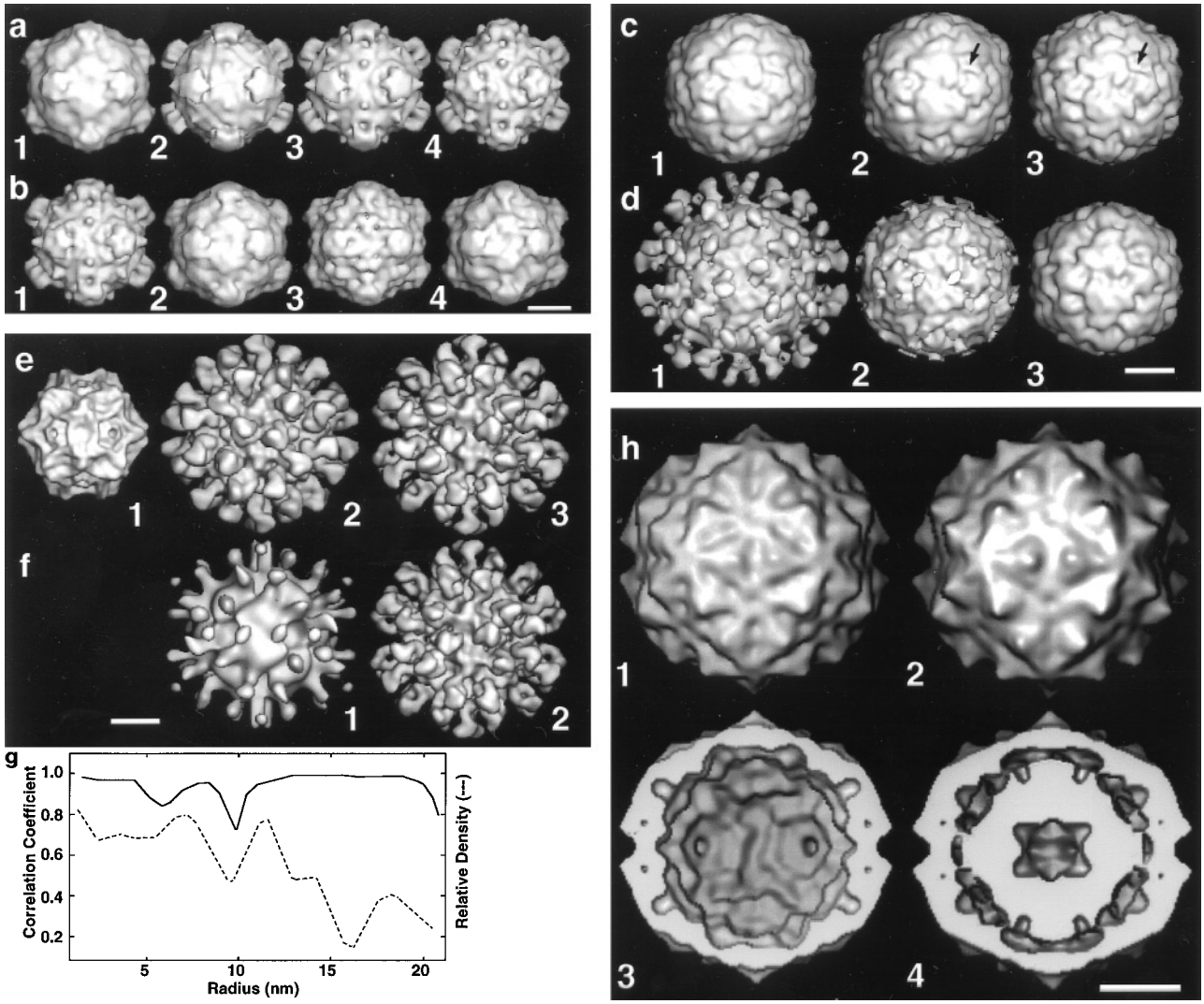

FIG. 5. (a) Refinement of ϕX174 with CPMV starting model and (b) refinement of CPMV with ϕX174 starting model. (a1) 3D reconstruction of CPMV (Porta *et al.*, 1994). (a2–a3) ϕX174 reconstructions obtained at intermediate stages of refinement. (a4) Final ϕX174 reconstruction computed from 15 images. (b1) 3D reconstruction of ϕX174 (Olson *et al.*, 1992). (b2–b3) CPMV reconstructions obtained at intermediate stages of refinement. (b4) Final CPMV reconstruction computed from 40 images. Note how details of the capsid surface such as the small protrusions on the threefold axes of ϕX174 appropriately emerge (a2–a4) or disappear (b1–b2) as the refinements proceed. (c) Refinement of HRV16 with HRV14 and (d) with HRV16 starting models. (c1) HRV16 X-ray model (Oliveria *et al.*, 1993). (c2) HRV14 X-ray model (Rossmann *et al.*, 1985). (c3) Final HRV16 reconstruction computed from 16 images and using the HRV14 model (c2) for PFT refinement. (d1) 3D reconstruction of HRV16/ICAM-1 complex (Olson *et al.*, 1993). (d2) The same as (d1) after all but the lowest radial portions of the ICAMs were computationally trimmed away. (d3) Final HRV16 reconstruction computed from 35 images and using the trimmed HRV16/ICAM model (d2) for PFT refinement. Arrows point to distinguishing features in the two serotypes of HRV (a ridge of density in HRV16 that is absent in HRV14). (e–g) Refinement of CPV–Fab complex with pseudo-atomic and single-particle reconstruction starting models. (e1) CPV X-ray model (Tsao *et al.*, 1991). (e2) Pseudo-atomic model of CPV–Fab made by docking 60 copies of the Fab(Kol) X-ray structure (Marquart *et al.*, 1980) onto the surface of the CPV X-ray model (e1) at positions consistent with the formation of escape mutants (Strassheim *et al.*, 1994). (e3) Final CPV–Fab reconstruction computed from 40 images and using model (e2) for PFT refinement. (f1) CPV–Fab reconstruction computed from one particle image (Wikoff *et al.*, 1994). (f2) Final CPV–Fab reconstruction computed from 40 images and using the single-particle reconstruction (f1) for PFT refinement. (g) Correlation coefficient plot (solid line) comparing reconstructions (e3) and (f2) as a function of particle radius. The radial density distribution of the average of (e3) and (f2) (dashed line) shows the high correlation between reconstructions (e3) and (f2) at all radii, including the Fab molecules (r = 14.5 to 21.5 nm). (h) Refinement of FHV images against FHV X-ray model. (h1) FHV X-ray model (Fisher and Johnson, 1993). (h2) Final refined FHV reconstruction computed from 17 images. (h3–h4) are cross-sections of (h1) and (h2), respectively, showing the far halves of each density map. Note how the bulk RNA (central, solid core) shows up in the reconstruction (h4) despite its absence in the starting model (h3). All the X-ray models (c1, e1, e2, h1, and h3) were computed at 2.5 nm resolution from atomic coordinates. Bars, 10 nm.

structure. Nonetheless, when a 3D reconstruction of CPMV (Porta *et al.*, 1994) was used as a starting reference model for the refinement of ϕX174 image data (Fig. 5a) or a 3D reconstruction of ϕX174 (Olson *et al.*, 1992) was used as a starting reference model for the refinement of CPMV image data (Fig. 5b), the

image data constrained the PFT refinement to yield final, correct structures.

Example 4: HRV14 and HRV16 Models—Analysis of HRV16

The atomic structures of several of the 114 serotypes of HRV (~30 nm diameter) have been determined (Rossmann, 1994). Despite several attempts, a 3D reconstruction of HRV was never accomplished by use of Common Lines methods (N. H. Olson, unpublished results). Lack of success was attributed to the extremely noisy nature of the HRV images and the overall smooth morphology of the protein capsid. However, a 3D reconstruction of HRV16 complexed with the N-terminal two domains of ICAM-1, the receptor molecule for the major group of HRV, was successfully obtained by means of Common Lines methods (Fig. 5d1; Olson *et al.*, 1993). This worked presumably because the ICAM molecules add significant surface features to the HRV structure. This 3D reconstruction, *after* the ICAM molecules were computationally trimmed off (Fig. 5d2), succeeded as a starting model for refinement of a data set of native HRV16 images and led to a 3D reconstruction of HRV16 (Fig. 5d3). As a further test, we used the X-ray structure of HRV14 (Fig. 5c2; Rossmann *et al.*, 1985) to compute a 2.5-nm-resolution model to refine the same HRV16 images. A similar 3D reconstruction of HRV16 resulted (Fig. 5c3). Comparison of these two reconstructions (Figs. 5c3 and 5d3) with a low-resolution representation of the HRV16 atomic structure (Fig. 5c1; Oliveria *et al.*, 1993) shows that HRV16 reconstructions indeed show very subtle yet genuine features that distinguish the two HRV serotypes. For example, a ridge of density in HRV16 that crosses the "canyon" surrounding the star-shaped pentamers (Fig. 5c3, arrow) is absent in HRV14 (Fig. 5c2, arrow).

Example 5: Analysis of CPV–Fab Complex

The atomic structures of CPV (25.5 nm diameter; Tsao *et al.*, 1991; Fig. 5e1) and several antibody Fab fragments (Wilson and Stanfield, 1993) are known. In the analysis of the binding of a neutralizing monoclonal antibody to a CPV epitope, two different models were used to obtain 3D reconstructions of the virus–Fab complex from the same set of cryoEM images (Wikoff *et al.*, 1994). One model (Fig. 5e2) was generated by docking the atomic model of Fab(Kol) (Marquart *et al.*, 1980) to the atomic structure of the native CPV (Fig. 5e1, Tsao *et al.*, 1991). The second model was obtained by applying the Common Lines method to a *single* CPV–Fab particle image to generate a low-resolution, "single-particle" 3D reconstruction (Venién-Bryan and Fuller, 1994) that showed "promising" features (i.e., lumps sticking out of the surface of a ball of density: Fig. 5f1). Both models led to virtually identical 3D reconstructions (Figs. 5e3, 5f2, and 5g). Close inspection of the "pseudo-atomic" model of the complex (Fig. 5e2) in hindsight showed that the Fab(Kol) model was placed in approximately the correct location with respect to the surface of CPV, but was ~60° off in its axial orientation. Thus, the incorrectness of the finer details of the pseudo-atomic model of the complex did not prevent the PFT routine from leading to a reliable 3D reconstruction.

Example 6: FHV X-Ray Model—FHV Analysis

For the spherical viruses whose atomic structures are known, it is mainly the highly ordered protein shell that is revealed. The nucleic acid is generally missing in X-ray maps because the bulk of the genome does not adopt icosahedral symmetry. In addition, X-ray diffraction data are seldom recorded or analyzed at resolutions *lower* than 1.5–2.0 nm. Nonetheless, the X-ray structure of the protein capsid still serves as an excellent model for PFT refinement of virion images (Fig. 5h). Indeed, the 3D reconstruction of the ssRNA, T = 3 insect virus, FHV (Figs. 5h2 and 5h4: Cheng *et al.*, 1994b), which was obtained by use of the *protein* portion of the X-ray model (Figs. 5h1 and 5h3: Fisher and Johnson, 1993), shows the distribution of the RNA (Fig. 5h4). A difference map, computed by subtracting the protein X-ray model from the EM map, showed highly ordered regions of RNA (data not shown) that corresponded exactly with the small portion of RNA that was seen in the original X-ray structure (Fisher and Johnson, 1993). Thus, this "control" experiment showed that even subtle, internal features emerge from the analysis of the cryoEM image data despite their absence in the starting model for the PFT analysis.

Example 7: Influence of Model on Results

The 3D reconstruction of the ssRNA, T = 4 insect virus NβV (~40 nm maximum diameter; Olson *et al.*, 1990) failed as a model for refining a set of FHV images with the PFT routines (Figs. 6a–6d). The reconstruction obtained after five cycles of refinement exhibited features that resembled both viruses (Fig. 6d) but was obviously wrong. Continued refinement led to no significant changes. The precise reasons for the failure are not known, although the magnification of the NβV reconstruction was carefully rescaled to maximize the fit with the smaller FHV (34 nm maximum diameter: Wery *et al.*, 1994). Apparently, the structure of NβV differs so significantly from that of FHV that the FHV images correlate poorly with the projected views of the NβV model. This "bad" model influences the PFT refinement and leads to a final solution that bears no resemblance to the initial model and is also incorrect.

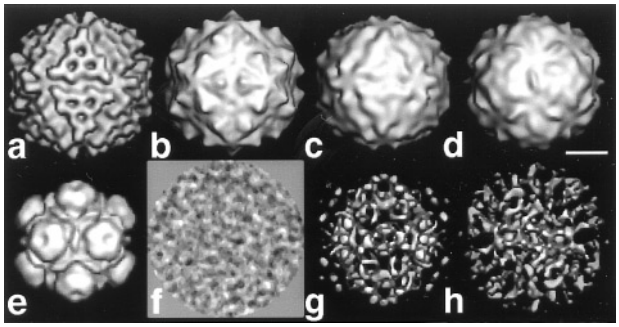

FIG. 6. Influence of model on results. (a–d) Refinement of FHV images against NβV model. (a) NβV 3D reconstruction (Olson *et al.*, 1990), rescaled to the size of FHV. (b) FHV 3D reconstruction (Cheng *et al.*, 1994b). (c) FHV reconstruction (includes 10 images) after first cycle of refinement. (d) Reconstruction of FHV computed from 17 images after five cycles of refinement. Though (d) contains some features that partially resemble both the starting model (a) and the expected result (b), it remains an unsatisfactory and incorrect result. Bar, 10 nm. (e–h) Refinement of pure noise data against a simple 3D model. (e) 3D computer model of T = 1 particles of polyoma capsid protein. (f) One of a 50-particle data set of "shot-noise" images. (g–h) 3D reconstructions obtained after the first and fourth cycles of PFT refinement, using (e) as starting model.

To further test the extent to which the model and image data influence the final results, we generated a data set of shot noise images (Fig. 6f) and refined these images against a 3D computer model of T = 1 particles of polyoma capsid protein (Fig. 6e). Despite repeated attempts, a 3D map that resembled the initial model was never obtained from these data (Figs. 6g–6h).

CONCLUSIONS

The last example serves as strong reminder that not just *any* model succeeds with the PFT analysis. Our experience with numerous 3D reconstructions clearly demonstrates though, that a model which "reasonably" mimics the image data can lead to a reliable 3D reconstruction (Table I). Under these conditions the PFT algorithm appears to be quite robust. If a particular reconstruction seems questionable, one can compute and compare the statistical significance of independent reconstructions (e.g., Milligan and Flicker, 1987), either starting with slightly different models and using the same images, or, if there are sufficient numbers of images, they can be subdivided and processed separately with the same model. The self-consistency of a set of images can also be checked by means of cross-common lines residual tests (Fuller, 1987).

The PFT method is a valuable adjunct to Common Lines procedures (Fuller *et al.*, 1996) because it provides rapid refinement and assessment of the quality of large numbers of images. Use of the PFT method in conjunction with spot-scan imaging and use of a field-emission, intermediate voltage microscope for recording high-resolution images (e.g., Olson *et al.*, 1995), raises the prospects for analyzing viral structures well beyond 2 nm resolution because it will be feasible to combine thousands of particle images. The prospects for adapting the PFT method

TABLE I
Virus Structures Solved by PFT Approach[a]

Solved structure	Initial PFT model
B19	Common Lines
B19	CPV X-ray
$CCMV_E$	CCMV
$CCMV_{RNA1}$	CCMV
CMV	$CCMV_S$
CPMV-IgG	CPMV-Fab
CPSMV	CPMV
CPV-Fab	Single-particle 3D
CPV-Fab	CPV X-ray + Kol X-ray
CRPV	Common Lines
FHV	FHV X-ray
FHV_{C74}	FHV
HPV_{L1}	HPV-1
HPV_{L1L2}	HPV-1
HRV16	$HRV16\text{-}ICAM_2$
HRV16	HRV14 X-ray
$HRV16\text{-}ICAM_5$	$HRV16\text{-}ICAM_2$
HRV14-IgG	HRV14-Fab
L-A	Common Lines
NOV	FHV
PBCV	Common Lines
Polyoma T = 1	SV40 pentamer X-ray
Polyoma T = 1	Single-particle 3D
$Reovirus_D$	$Reovirus_L$
$Reovirus_D\ V_E$	$Reovirus_L\ V_{CR}$
$Reovirus_D\ ISVP_E$	$Reovirus_L\ ISVP_{CR}$
$Reovirus_D\ C_E$	$Reovirus_L\ C_{CR}$
RRV	Common Lines
RRV-Fab	RRV
SNV-Fab	RRV-Fab
UmV	Single particle 3D
$\phi X174_{PV}$	$\phi X174_{PC}$

[a] Table lists selected examples of virus structure determinations performed strictly in our lab in which the PFT method was an integral part of the data analysis. These examples illustrate the variety of different initial models that can be successfully employed in the PFT refinement procedures. "Common Lines" signifies that the starting model for PFT refinement was a preliminary (typically low-resolution or with a limited set of images) 3D reconstruction that was computed with Common Lines (Crowther, 1971) and Modified Common Lines (Fuller, 1987; Fuller *et al.*, 1996) procedures. "Single-particle 3D" signifies that the model for PFT analysis was a low-resolution 3D reconstruction computed from an image of a single particle whose view orientation parameters, (θ, ϕ, ω), were estimated by the Common Lines method (Venién-Bryan and Fuller, 1994). "X-ray" signifies that the initial PFT model was derived from the atomic coordinates of a virus whose structure was solved at high resolution by X-ray crystallography. All remaining models were 3D reconstructions computed by Fourier-Bessel techniques (Fuller *et al.*, 1996) of viruses whose structure was believed to be similar to the virus being examined. Although most of these examples are from unpublished studies, the structure determinations of the following viruses have been reported: $CCMV_E$ (Zhao *et al.*, 1995), CPV–Fab (Wikoff *et al.*, 1994), FHV (Cheng *et al.*, 1994b), HPV_{L1L2} and HPV_{L1} (Hagensee *et al.*, 1994), L-A and UmV (Cheng *et al.*, 1994a), RRV (Cheng *et al.*, 1995), and $\phi X174_{PV}$ (Ilag *et al.*, 1995).

to study other macromolecular structures, including those that are nonspherical and nonsymmetrical, are good but will require that initial particle origins be determined separately and not refined against the average model projection. Subsequent refinement of origins could proceed normally after the initial orientations are determined.

This work was supported with grants from the NSF (MCB-9206305) and NIH (GM33050 and AI35212) to T.S.B. We gratefully acknowledge our colleagues: N. Olson, G. Wang, J. Johnson, T. Smith, M. Rossmann, R. Kuhn, and M. Young, whose inspiration, determination, and expertise made these studies possible; D. Belnap, J. Conway, K. Dryden, and S. Fuller for their willingness to both test and improve the EMPFT code; J. Tesmer for performing key feasibility tests of the original program; D. Belnap and S. Fuller for insightful comments on the manuscript; and G. Harauz for bringing to our attention his earlier work on orientation search procedures.

REFERENCES

Baker, T. S. (1992) Cryo-electron microscopy and three-dimensional image reconstruction of icosahedral viruses, *in 10th Eur. Congr. Electron Microsc.* (*Granada*) Vol. 3; pp. 275–279.

Baker, T. S., Drak, J., and Bina, M. (1988) Reconstruction of the three-dimensional structure of simian virus 40 and visualization of the chromatin core, *Proc. Natl. Acad. Sci. USA* **85,** 422–426.

Baker, T. S., Drak, J., and Bina, M. (1989) The capsid of small papova viruses contains 72 pentameric capsomeres: Direct evidence from cryo-electron microscopy of simian virus 40, *Biophys. J.* **55,** 243–253.

Belnap, D. M., Grochulski, W. D., Olson, N. H., and Baker, T. S. (1993) Use of radial density plots to calibrate image magnification for frozen-hydrated specimens, *Ultramicroscopy* **48,** 347–358.

Cheng, R. H., Olson, N. H., Baker, T. S. (1992) Cauliflower mosaic virus, a 420 subunit (T = 7), multilayer structure, *Virology* **186,** 655–668.

Cheng, R. H., Caston, J. R., Wang, G. J., Gu, F., Smith, T. J., Baker, T. S., Bozarth, R. F., Trus, B. L., Cheng, N., Wickner, R. B., and Steven, A. C. (1994a) Fungal virus capsids: Cytoplasmic compartments for the replication of double-stranded RNA formed as icosahedral shells of asymmetric Gag dimers, *J. Mol. Biol.* **244,** 255–258.

Cheng, R. H., Reddy, V., Olson, N. H., Fisher, A., Baker, T. S., and Johnson, J. E. (1994b) Functional implications of quasi-equivalence in a T = 3 icosahedral animal virus established by cryo-electron microscopy and X-ray crystallography, *Structure* **2,** 271–282.

Cheng, R. H., Kuhn, R. J., Olson, N. H., Rossmann, M. G., Choi, H.-K., Smith, T. J., and Baker, T. S. (1995) Three-dimensional structure of an enveloped alphavirus with T = 4 icosahedral symmetry, *Cell* **80,** 621–630.

Conway, J. F., Duda, R. L., Cheng, N., Hendrix, R. W., and Steven, A. C. (1995) Proteolytic and conformational control of virus capsid maturation: The bacteriophage HK97 system, *J. Mol. Biol.* **253,** 86–99.

Crowther, R. A. (1971) Procedures for three-dimensional reconstruction of spherical viruses by Fourier synthesis from electron micrographs, *Philos. Trans. R. Soc. London Ser. B.* **261,** 221–230.

Crowther, R. A., Amos, L. A., Finch, J. T., DeRosier, D. J., and Klug, A. (1970) Three dimensional reconstructions of spherical viruses by Fourier synthesis from electron micrographs, *Nature* (*London*) **226,** 421–425.

Crowther, R. A., and Amos, L. A. (1971) Harmonic analysis of electron microscope images with rotational symmetry, *J. Mol. Biol.* **60,** 123–130.

Crowther, R. A., and Amos, L. A., (1972) Three-dimensional image reconstruction of some small spherical viruses, *Cold Spring Harbor Symp. Quant. Biol.* **36,** 489–494.

Crowther, R. A., Kiselev, N. A., Böttcher, B., Berriman, J. A., Borisova, J. P., Ose, V., and Pumpens, P. (1994) Three-dimensional structure of hepatitis B virus core particles determined by electron cryomicroscopy, *Cell* **77,** 943–950.

Dokland, T., and Murialdo, H. (1993) Structural transitions during maturation of bacteriophage lambda capsids, *J. Mol. Biol.* **233,** 682–694.

Finch, J. T. (1972) The hand of the helix of tobacco mosaic virus, *J. Mol. Biol.* **66,** 291–294.

Fisher, A. J., and Johnson, J. E. (1993). Ordered duplex RNA controls capsid architecture in an icosahedral animal virus, *Nature* (*London*) **361,** 176–179.

Fuller, S. D. (1987) The T = 4 envelope of Sindbis virus is organized by interactions with a complementary T = 3 capsid, *Cell* **48,** 923–934.

Fuller, S. D., Berriman, J. A., Butcher, S. J., and Gowen, B. E. (1995) Low pH induces swiveling of the glycoprotein heterodimers in the Semliki Forest virus spike complex, *Cell* **81,** 715–725.

Fuller, S. D., Butcher, S. J., Cheng, R. H., and Baker, T. S. (1996) Three-dimensional reconstruction of icosahedral particles—The uncommon line, *J. Struct. Biol.* **116,** 48–55.

Griffith, J. P., Griffith, D. L., Rayment, I., Murakami, W. T. and Caspar, D. L. D. (1992) Inside polyomavirus at 25 Å resolution, *Nature* (*London*) **355,** 652–654.

Hagensee, M., Olson, N. H., Baker, T. S., and Galloway, D. (1994) Three-dimensional structure of vaccinia virus-produced HPV-1 capsids, *J. Virol.* **68,** 4503–4505.

Harauz, G., and van Heel, M. (1986) Direct 3D reconstruction from projections with initially unknown angles, *in* Gelsema, E. S. and Kanal L. N. (Eds.), Pattern Recognition in Practice II, pp. 279–288, Elsevier, North-Holland.

Ilag, L. L., Olson, N. H., Dokland, T., Music, C. L., Cheng, R. H., Bowen, Z., McKenna, R., Rossmann, M. G., Baker, T. S., and Incardona, N. L. (1995) DNA packaging intermediates of bacteriophage ϕX174, *Structure* **3,** 353–363.

Kenney, J. M., Sjoberg, M., Garoff, H., and Fuller, S. D. (1994) Visualization of fusion activation in the Semliki Forest virus spike, *Structure* **2,** 823–832.

Klug, A., and Finch, J. T. (1968) Structure of viruses of the papilloma-polyoma type. IV. Analysis of tilting experiments in the electron microscope, *J. Mol. Biol.* **31,** 1–12.

Lake, J. A. (1972) Biological studies, *in* Lipson, H. (Ed.), Optical Transforms, pp. 153–188, Academic Press, New York.

Marquart, M., Deisenhofer, J., Huber, R. and Palm, W. (1980) Crystallographic refinement and atomic models of the intact immunoglobulin molecule Kol and its antigen-binding fragment at 3.0 Å and 1.9 Å resolution, *J. Mol. Biol.* **141,** 369–391.

Martino, R. J., Johnson, C. A., Suh, E. B., Trus, B. L., and Yap, T. K. (1994). Parallel computing in biomedical research, *Science* **265,** 902–908.

McKenna, R., Xi, D., Willingmann, P., Ilag, L. L., Krishnaswamy, S., Rossmann, M. G., Olson, N. H., Baker, T. S., and Incardona, N. L. (1992) The atomic structure of the single-stranded DNA bacteriophage ϕX174 and its functional implications, *Nature* (*London*) **355,** 137–143.

Milligan, R. A., and Flicker, P. F. (1987) Structural relationships of actin, myosin, and tropomyosin revealed by cryo-electron microscopy, *J. Cell. Biol.* **105,** 29–39.

Misell, D. L. (1978) Image analysis, enhancement and interpretation, *Pract. Methods Electron Microsc.* (Glauert A. M. Ed.) **7,** 1–305.

Moody, M. F. (1990) Image analysis of electron micrographs, *in* Hawkes, P. W., and Valdre, U. (Eds.), Biophysical Electron Microscopy: Basic Concepts and Modern Techniques, pp. 145–287, Academic Press, New York.

Oliveria, M. A., Zhao, R., Lee, W. M., Kremer, M., Minor, I., Rueckert, R. R., Diana, G. D., Pevear, D. C., Dutko, F. J., McKinlay, M. A., and Rossmann, M. G. (1993) The structure of human rhinovirus 16, *Structure* **1,** 51–68.

Olson, N. H., and Baker, T. S. (1989) Magnification calibration and the determination of spherical virus diameters using cryomicroscopy, *Ultramicroscopy* **30,** 281–297.

Olson, N. H., Baker, T. S., Johnson, J. E., and Hendry, D. A. (1990) The three-dimensional structure of frozen-hydrated *Nudaurelia capensis* β, a T = 4 insect virus, *J. Struct. Biol.* **105,** 111–122.

Olson, N. H., Baker, T. S., Willingmann, P., and Incardona, N. L. (1992) The three-dimensional structure of frozen-hydrated bacteriophage ϕX174, *J. Struct. Biol.* **108,** 168–175.

Olson, N. H., Kolatkar, P. R., Oliveria, M. A., Cheng, R. H., Greve, J. M., McClelland, A., Baker, T. S., and Rossmann, M. G. (1993) Structure of a human rhinovirus complexed with its receptor molecule, *Proc. Natl. Acad. Sci. USA* **90,** 507–511.

Olson, N. H., Lücken, U., Walker, S. B., Otten, M. T., and Baker, T. S. (1995) Cryoelectron microscopy and image reconstruction of spherical viruses with spot scan and FEG technologies, *Proc. Microsc. Microanal.* (*Kansas City*) **53,** 1086–1087.

Penczek, P. A., Grassucci, R. A., and Frank, J. (1994) The ribosome at improved resolution: New techniques for merging and orientation refinement in 3D cryo-electron microscopy of biological particles, *Ultramicroscopy* **53,** 251–270.

Porta, C., Wang, G., Cheng, R. H., Chen, Z., Baker, T. S., and Johnson, J. E., (1994) Direct imaging of interactions between an icosahedral virus and conjugate F_{ab} fragments by cryoelectron microscopy and X-ray crystallography, *Virology* **204,** 777–788.

Radermacher, M. (1994) Three-dimensional reconstruction from random projections: Orientational alignment via Radon transforms, *Ultramicroscopy* **53,** 121–136.

Rayment, I., Baker, T. S., Caspar, D. L. D., and Murakami, W. R. (1982) Polyoma virus capsid crystal structure at 22.5 Å resolution, *Nature* **295,** 110–115.

Rayment, I., Baker, T. S. and Caspar, D. L. D. (1983) A description of the techniques and application of molecular replacement used to determine the structure of polyoma virus capsids at 22.5 Å resolution, *Acta Crystallogr.* **B39,** 505–516.

Rossmann, M. G. (1972) The Molecular Replacement Method, Gordon & Breach, New York.

Rossmann, M. G. (1994) Viral cell recognition and entry, *Protein Sci.* **3,** 1712–1725.

Rossmann, M. G., Arnold, E., Erickson, J. W., Frankenberger, G., Griffith, J. P., Hecht, H. J., Johnson, J. E., Kamer, G., Luo, M., Mosser, A. G., Rueckert, R. R., Sherry, B., and Vriend, G. (1985) Structure of a human common cold virus and functional relationship to other picornaviruses, *Nature* (*London*) **317,** 145–153.

Schatz, M., and van Heel, M. (1990) Invariant classification of molecular views in electron micrographs, *Ultramicroscopy* **32,** 255–264.

Smith, T. J., Olson, N. H., Cheng, R. H., Liu, H., Chase, E. S., Lee, W. M., Leippe, D. M., Mosser, A. G., Rueckert, R. R., and Baker, T. S. (1993a) Structure of human rhinovirus complexed with F_{ab} fragments from a neutralizing antibody, *J. Virol.* **67,** 1148–1158.

Smith, T. J., Olson, N. H., Cheng, R. H., Chase, E. S., and Baker, T. S. (1993b) Structure of a human rhinovirus-bivalently bound antibody complex: Implications for virus neutralization and antibody flexibility, *Proc. Natl. Acad. Sci. USA,* **90,** 7015–7018.

Stauffacher, C. V., Usha, R., Harrington, M., Schmidt, T., Hosur, M. V., and Johnson, J. E. (1987) The structure of cowpea mosaic virus at 3.5 Å resolution, *in* Moras (Ed.), Crystallography in Molecular Biology, pp. 293–308, Plenum, New York.

Strassheim, M. L., Gruenberg, A., Veijalainen, P., Sgro, J. Y., and Parrish, C. R. (1994) Two dominant neutralizing antigenic determinants of canine parovirus are found on the threefold spike of the virus capsid, *Virology* **198,** 175–184.

Tsao, J., Chapman, M. S., Agbandje, M., Keller, W., Smith, K., Wu, H., Luo, M., Smith, T. J., Rossmann, M. G., Compans, R. W., and Parrish, R. W. (1991) The three dimensional structure of canine parvovirus and its functional implications, *Science* **251,** 1456–1464.

Venién-Bryan, C., and Fuller, S. D. (1994). The organization of the spike complex of Semliki Forest virus, *J. Mol. Biol.* **236,** 572–583.

Wang, G., Porta, C., Chen, Z., Baker, T. S., and Johnson, J. E. (1992) Identification of a F_{ab} interaction site (footprint) on an icosahedral virus by cryo-electron microscopy and X-ray crystallography, *Nature* (*London*) **355,** 275–278.

Wery, J-P., Reddy, V. S., Hosur, M. V., and Johnson, J. E. (1994) The refined three-dimensional structure of an insect virus at 2.8 Å resolution, *J. Mol. Biol.* **235,** 565–586.

Wikoff, W. R., Wang, G., Parrish, C. R., Cheng, R. H., Strassheim, M. L., Baker, T. S., and Rossmann, M. G. (1994) Structures of a neutralized virus: Canine parvovirus complexed with neutralizing antibody fragments, *Structure* **2,** 595–607.

Wilson, I. A., and Stanfield, R. L. (1993) Antibody-antigen interactions, *Curr. Opin. Struc. Biol.* **3,** 113–118.

Zhao, X., Fox, J., Olson, N. H., Baker, T. S., and Young, M. J. (1995) *In vitro* assembly of cowpea chlorotic mottle virus from coat protein expressed in *E. coli* and *in vitro* transcribed viral cDNA, *Virology* **207,** 486–494.